Compact Reconnaissance Imaging Spectrometer observations of water vapor and carbon monoxide

Michael D. Smith,[1] Michael J. Wolff,[2] R. Todd Clancy,[2] and Scott L. Murchie[3]

Received 26 October 2008; revised 16 March 2009; accepted 9 April 2009; published 10 June 2009.

[1] The Compact Reconnaissance Imaging Spectrometer for Mars (CRISM) onboard the Mars Reconnaissance Orbiter (MRO) spacecraft began taking observations in September 2006 and has now collected more than a full Martian year of data. Retrievals performed using the near-infrared spectra obtained by CRISM are used to characterize the seasonal and spatial variation of the column abundance of water vapor and the column-averaged mixing ratio of carbon monoxide. CRISM retrievals show nominal behavior in water vapor during northern hemisphere spring and summer with maximum abundance reaching 50 precipitable micrometers. Water vapor abundance during the southern hemisphere spring and summer appears significantly reduced compared to observations by other instruments taken during previous years. The CRISM retrievals show the seasonally and globally averaged carbon monoxide mixing ratio to be 700 ppm, but with strong seasonal variations at high latitudes. The summertime near-polar carbon monoxide mixing ratio falls to 200 ppm in the south and 400 ppm in the north as carbon dioxide sublimates from the seasonal polar ice caps and dilutes noncondensable species including carbon monoxide. At low latitudes, the carbon monoxide mixing ratio varies in response to the mean seasonal cycle of surface pressure.

Citation: Smith, M. D., M. J. Wolff, R. T. Clancy, and S. L. Murchie (2009), Compact Reconnaissance Imaging Spectrometer observations of water vapor and carbon monoxide, *J. Geophys. Res.*, *114*, E00D03, doi:10.1029/2008JE003288.

1. Introduction

[2] There has been a long history of observations of water vapor abundance using spacecraft at Mars because of the importance of the water cycle in understanding the Martian climate (see *Smith* [2008] for an overview of spacecraft observations of water vapor at Mars). A baseline of water vapor observations made by Viking IRTM [*Jakosky and Farmer*, 1982], Mars Global Surveyor TES [*Smith*, 2002, 2004], and Mars Express instruments [e.g., *Fouchet et al.*, 2007; *Melchiorri et al.*, 2007; *Fedorova et al.*, 2006], have provided a good, initial characterization of the seasonal and spatial trends. However, it is also clear from the observations that there is some interannual variation in water vapor abundance and that additional observations would provide valuable new information.

[3] In comparison to water vapor, there have been relatively few observations of carbon monoxide at Mars. Observations by Phobos ISM [*Rosenqvist et al.*, 1992], Mars Express OMEGA [*Encrenaz et al.*, 2006], and ground-based observers [e.g., *Clancy et al.*, 1990; *Lellouch et al.*, 1991; *Krasnopolsky*, 2003, 2007] show an average abundance of about 700 ppm with possible variations, but a full seasonal and spatial characterization of carbon monoxide abundance has not yet been published. As a noncondensable species, the abundance of carbon monoxide and its variation with season and location provide important clues about atmospheric transport dynamics [e.g., *Nelli et al.*, 2007; F. Forget et al., Non-condensable gas enrichment and depletion in the Martian polar regions, paper presented at Third Workshop on Mars Modeling and Observations, Lunar and Planetary Institute, Williamsburg, Virginia, 2008].

[4] Near-infrared spectra returned by the Compact Reconnaissance Imaging Spectrometer for Mars (CRISM), carried onboard the Mars Reconnaissance Orbiter (MRO) [*Murchie et al.*, 2007] contain the clear spectral signature of several atmospheric gases including carbon dioxide, water vapor, and carbon monoxide. These observations, which now cover a time span of more than one full Martian year, allow the seasonal and spatial variation of both water vapor and carbon monoxide to be characterized. The water vapor observations extend the climatological record of previous observations and provide complementary information to concurrent observations from Mars Express instruments and the MRO Mars Climate Sounder instrument. The carbon monoxide observations provide the first characterization of its seasonal and spatial variations over a full Martian year and for a wide range of latitudes.

[5] In this paper we present the results of retrievals of water vapor and carbon monoxide abundance in the Martian atmosphere using spectra taken by the CRISM instrument during the first full Martian year of MRO operations. In section 2, we discuss the CRISM data instrument and data

[1]NASA Goddard Space Flight Center, Greenbelt, Maryland, USA.
[2]Space Science Institute, Boulder, Colorado, USA.
[3]Johns Hopkins University Applied Physics Laboratory, Laurel, Maryland, USA.

0148-0227/09/2008JE003288

set. Details of the retrieval algorithm including an estimate of uncertainties are given in section 3. In section 4, we present the results of the retrievals, and those results are compared with other observations in section 5.

2. Data Set

[6] The Mars Reconnaissance Orbiter (MRO) arrived at Mars in March 2006, completed aerobraking in August 2006, and began its Primary Science Phase in November 2006. MRO operates from a sun-synchronous, near-polar, near-circular (~300 km altitude) orbit with a mean local solar time of about 0300 and 1500 LT [*Zurek and Smrekar*, 2007].

2.1. CRISM Instrument

[7] The Compact Reconnaissance Imaging Spectrometer for Mars (CRISM) is a hyperspectral imager with a spatial resolution of 15–19 m/pixel and a spectral range of 362–3920 nm with a spectral sampling of 6.55 nm and a spectral resolution in the infrared (~2000 nm) of about 15 nm [*Murchie et al.*, 2007]. Gimbals allow off-nadir pointing in both the along-track and cross-track directions. There are two detector arrays with 640 spatial pixels across track and 480 spectral pixels. One detector covers visible to near-infrared wavelengths (362–1056 nm), while the other covers infrared wavelengths (1001–3920 nm). Hyperspectral images are built up using a combination of orbital motion and gimbal movements. The ability for onboard spatial binning and the selection of specific spectral channels allows the data rate from CRISM to be managed for maximum scientific return. The primary spectral sampling modes return either 545 channels ("hyperspectral" observations) at the full instrument spectral resolution, or a 72-channel subset ("multispectral" observations) of the channels chosen to define surface and atmospheric features of interest [*Pelkey et al.*, 2007].

2.2. Observation Types

[8] There are three main types of observations performed by CRISM. The first are a set of hyperspectral (full spectral resolution) images taken as an emission phase function (EPF), where the same area on the surface is imaged at a wide range of emission angles as the spacecraft passes over the site. The typical EPF sequence includes 11 images, with five taken inbound at emission angles between roughly 30 and 70°, one image taken at nadir (near zero emission angle as MRO passes over the site), and five more images taken outbound at emission angles between roughly 30 and 70°. The purpose of the EPF sequence is to allow the separation of the contributions to the observed signal from the atmosphere and the surface [*Clancy and Lee*, 1991; *Clancy et al.*, 2003; *Wolff et al.*, 2009; *McGuire et al.*, 2008]. Most of the hyperspectral EPF images are taken at locations of interest to surface science, although a grid of EPFs covering the globe is taken approximately every two weeks for the purpose of monitoring atmospheric phenomena (S. Murchie et al., CRISM investigation and data set from the Mars Reconnaissance Orbiter's primary science phase, submitted to *Journal of Geophysical Research*, 2009). Depending on available spacecraft resources and data rate, as many as two dozen EPF observations can be taken during a single day. In practice, the combination of the EPFs targeted at surface features and those taken as part of the atmospheric grids provide enough coverage to well-characterize the seasonal, global-scale trends of atmospheric gases, but are not enough to provide daily (or even weekly) maps of abundances.

[9] The other two types of CRISM observations are taken in the nadir geometry only, without the accompanying EPF images. One type of these nadir observations is taken as hyperspectral images, while the other is taken as multispectral images. In both cases, these images are spatially binned and are generally taken in strips along the orbit track at times when there are no EPF targets available and when spacecraft resources allow. The goal of the multispectral nadir images in particular is to map the entire surface of Mars at 100–200 m resolution over the lifetime of the MRO mission [*Murchie et al.*, 2007].

2.3. Observations Used

[10] It is possible to retrieve gas abundance from both the hyperspectral and multispectral observations, but having the full spectral information available allows much lower uncertainties in results, so for this paper we use only the CRISM hyperspectral data (both EPF and nadir-only). Having a full EPF is critical for determination of aerosol optical thickness and scattering properties [see *Wolff et al.*, 2009]. However, for the retrieval of gas abundance, numerical experiments show that the additional information contained in the ten off-nadir images of the EPF is relatively small. Therefore, we have decided to use only the central, nadir image of each EPF in our retrieval. This considerably reduces computational time since we need only compute synthetic radiance for one emission angle instead of eleven, and it also allows us to include the hyperspectral nadir-only observations on an equal footing with the EPF observations, which provides a significant augmentation to the number of observations available for this study.

[11] For each CRISM EPF observation we spatially average the central 100 × 100 pixels of the nadir image to form the spectrum we use in the retrieval. This translates to an area about 2 km square on the surface. In this study we are interested in looking at seasonal and large-scale (regional to global scale) spatial trends in gas abundance, so we do not need pixel-by-pixel resolution. The spatial averaging also reduces random noise in the spectra. Taking the central 100 pixels in the cross-track direction also limits the small change in wavelength for a given channel from one end of the image to the other (known as "spectral smile"). The hyperspectral nadir-only observations are handled in a similar way. A spatial average of the central 100 × 100 pixels in each image is taken for use in the retrieval.

[12] At the wavelengths used in this study (1800–2600 nm) there is negligible contribution from thermal radiation, so we rely on reflected solar light for our signal. This means that we cannot view the winter polar regions. We also wish to avoid the complications of radiative transfer near the limb, so we limit our retrieval to observations with a solar incidence angle of 80° or less. We also do not attempt retrieval on any spectrum that shows the spectral signatures of surface ice (e.g., S. Cull et al., Seasonal H_2O and CO_2 ices at the Mars Phoenix landing site: Results from prelanding CRISM and HiRISE observations, submitted to *Journal of Geophysical Research*, 2009).

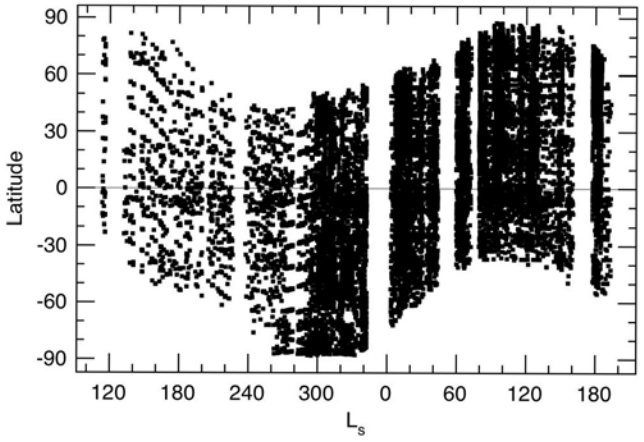

Figure 1. The seasonal (L_s) and latitudinal distribution of CRISM retrievals. Gaps near the winter poles are from the requirement that solar incidence angle be no larger than 80° and that the ground be free of surface ice. Vertical gaps were caused by solar conjunction and recovery from spacecraft anomalies.

[13] For this study, we use all CRISM hyperspectral images, both EPF and nadir-only. The first CRISM EPFs were taken on 27 September 2006 (Mars Year 28, L_s = 113°) during the instrument checkout period after the completion of aerobraking but before the beginning of the Primary Science Phase (PSP) of the mission. More regular EPF observations began after the beginning of the PSP on 8 November 2006 (Mars Year 28, L_s = 132°). Hyperspectral nadir-only observations began 5 August 2007 (Mars Year 28, L_s = 290°). Both types of observations continue to be taken at the time of this writing. In this paper we include all observations taken through 17 January 2009 (Mars Year 29, L_s = 193°), which gives over one full Martian year of data. Included in this data set are retrievals from approximately 9200 EPF observations and 5900 hyperspectral nadir-only (spatially averaged) observations.

[14] Figure 1 shows the seasonal and latitudinal distribution of the observations used in this study. Other than the unavoidable lack of observations in the winter polar regions there is good coverage for all seasons and latitudes. A few short gaps in the data record were caused by solar conjunction or recovery from spacecraft anomalies.

2.4. Typical CRISM Spectrum

[15] Figure 2 shows part of a typical CRISM spectrum (100 × 100 pixel spatial average) used in this study. This particular spectrum comes from an EPF observation taken at low latitudes during southern hemisphere spring (observation HRL0000515F, Mars Year 28, L_s = 211°, 9°S latitude, 193°W longitude). Here the observed radiance has been divided by the solar spectrum to better show spectral features coming from the Martian surface and atmosphere. While the entire CRISM spectrum covers the spectral range 362–3920 nm, we show here only that part relevant for this retrieval. As the main constituent of the atmosphere, carbon dioxide has numerous strong spectral signatures that are readily apparent in the spectrum, including prominent bands centered near wavelengths of 1400, 2000, and 2700 nm. We choose to use the band centered near 2000 nm for our retrieval of carbon dioxide abundance because it provides the best balance between having sufficient strength to provide good signal, while not being so strong that the band is completely saturated. The major spectral signatures caused by water vapor are centered at roughly 1350, 1900, and 2600 nm. The band at 1350 nm is relatively weak, but the bands at 1900 and 2600 nm are both mixed with stronger carbon dioxide bands on their long-wavelength edges. Our experience with the CRISM spectra is that the band at 2600 nm (which is the strongest of the three) provides the most reliable retrieval of water vapor abundance. Carbon monoxide has a readily apparent spectral signature centered near 2350 nm. Although this band is weak, it is isolated from other atmospheric spectral signatures and still provides reliable retrievals.

3. Retrieval Algorithm

[16] Radiative transfer modeling of CRISM spectra has been used to retrieve the column abundance of water vapor,

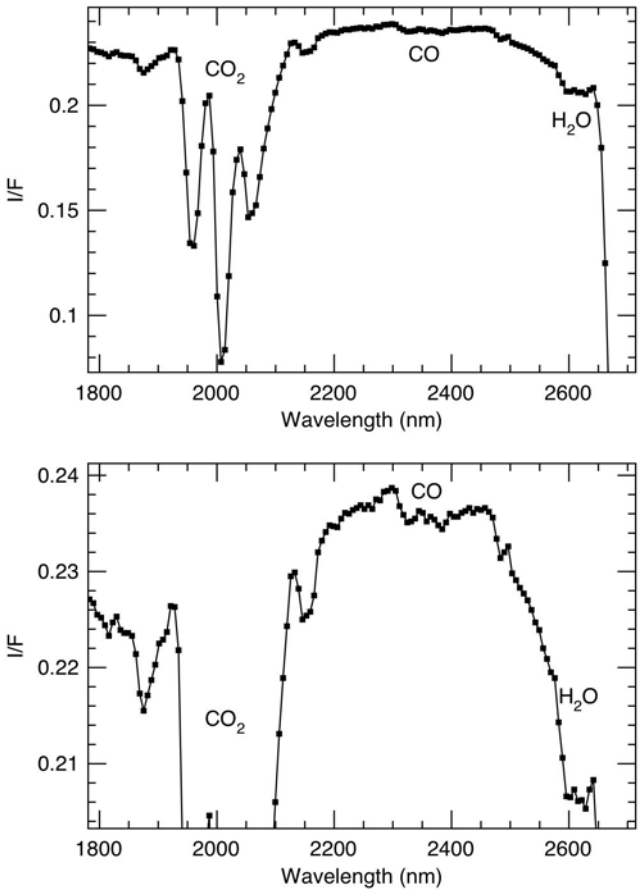

Figure 2. A portion of a typical CRISM spectrum used in the retrieval. Spectral features caused by CO_2, CO, and H_2O are labeled. (top) This is one spatially averaged near-nadir spectrum from CRISM observation HRL0000515F (L_s = 211°, 9°S latitude, 193°W longitude). (bottom) Same spectrum, but zoomed in to better show the CO and H_2O features. The entire CRISM spectrum covers 362–3920 nm, and there are 11 images taken at different emission angles making up the entire observation.

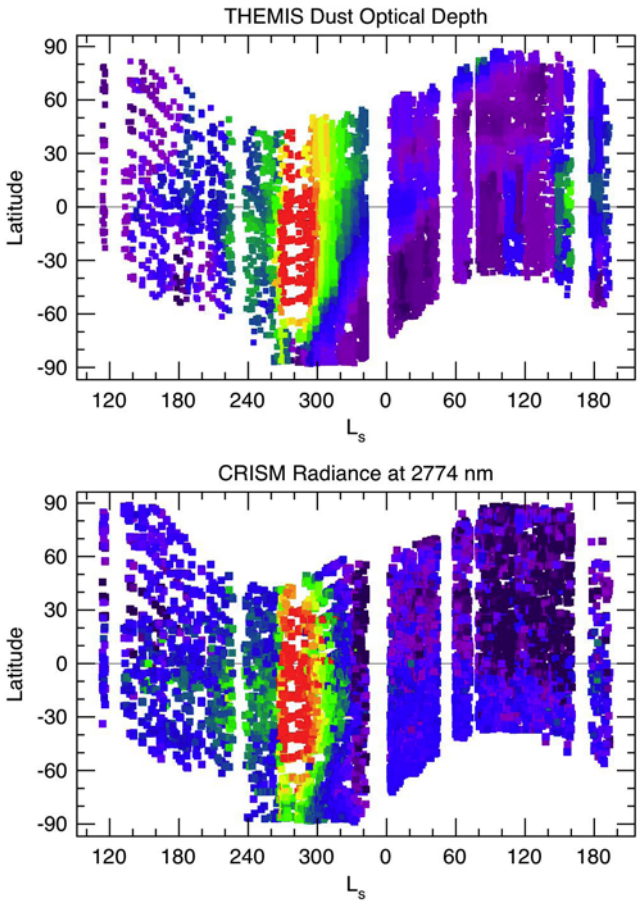

Figure 3. (top) Dust optical depth observed by THEMIS, sampled at the times and locations of the CRISM observations. The color scale goes from (thermal infrared) dust optical depth of zero (purple) to 1.0 or greater (red). Note the planet-encircling dust storm between $L_s = 270°$ and 305°. (bottom) Radiance observed by CRISM at 2774 nm within the very strong CO_2 absorption band, which is indicative of dust. The correspondence between the two validates the use of THEMIS observations of dust for this retrieval.

carbon monoxide, and carbon dioxide. The basic idea is to vary gas abundance until a best fit is achieved between the computed and observed spectrum in the spectral region of the gas absorptions. This process is explained in more detail below.

3.1. Radiative Transfer and Assumptions

[17] We compute synthetic spectra using the correlated-k approximation for gas absorption [*Lacis and Oinas*, 1991] with line parameters from the HITRAN 2004 spectroscopic database [*Rothman et al.*, 2005]. A discrete ordinates approach [see *Thomas and Stamnes*, 1999] is used to treat aerosol scattering and the solar beam.

[18] The quantities retrieved are the gas abundances of carbon dioxide, carbon monoxide, and water vapor, the equivalent Lambert albedo of the "continuum" spectral regions between gas absorptions, and a wavelength calibration of the CRISM channels. The viewing geometry, including the incidence angle, emission angle, and distance between Mars and the Sun, is taken from spacecraft records and is assumed to be well known. The solar spectrum used is that adopted by the CRISM team, which is taken from the terrestrial MODTRAN atmospheric radiation code [*Berk et al.*, 1998]. The surface temperature and atmospheric temperature profile (which affect the absorption coefficients of the modeled gases) are taken from TES climatology [*Smith*, 2004] from the first Martian year of TES operations (roughly Mars Year 24, $L_s = 120°$ to Mars Year 25, $L_s = 120°$). Surface pressure is computed using the retrieved abundance of carbon dioxide and an assumed CO_2 volume mixing ratio of 0.9532 [*Owen et al.*, 1977]. The vertical distribution of carbon monoxide is assumed to be well mixed. Water vapor is assumed to be well mixed up to the water condensation level and then follow the water saturation curve above that.

[19] Aerosol optical depth can be either estimated using climatological values observed by Mars Global Surveyor TES [*Smith*, 2004, 2008], concurrent observations by Mars Odyssey THEMIS [*Smith et al.*, 2003], or by direct retrieval from CRISM EPF observations [*Wolff et al.*, 2009]. Here we have chosen to use THEMIS observations because of their greater availability during the development of this algorithm. As will be discussed below further in section 3.4, an error in the assumed aerosol optical depth does not lead to significant uncertainties in the retrieved results unless the error is large. While using TES climatology values may be risky during the perihelion season when large dust storms may occur, using concurrent THEMIS observations captures the actual global-scale, seasonal variation of aerosols and is quite sufficient for the purposes of this retrieval.

[20] Figure 3 (top) shows the seasonal and latitudinal variation of dust optical depth as observed by THEMIS and used in this retrieval of CRISM data. Of particular note is the planet-encircling dust storm that occurred between roughly $L_s = 270°$ and 305° (Mars Year 28, July–August 2007). The THEMIS observations of dust optical depth can be compared against the radiance observed by CRISM at 2774 nm. That wavelength lies within an extremely strong CO_2 band so that the observed radiance is dominated by light scattered by dust aerosols (especially those high in the atmosphere). Figure 3 (bottom) shows the seasonal and latitudinal variation of CRISM radiance at 2774 nm, which gives a rough indication of when and where there was significant dust loading. The correspondence between the THEMIS and CRISM observations of dust is very good, validating the use of the THEMIS observations for the CRISM retrieval.

[21] The dust size distribution and aerosol indices of refraction are taken from the results of CRISM analysis by *Wolff et al.* [2009]. Dust is assumed to be well mixed with the background gas, while water ice clouds are assumed to be composed of 2-micron particles well mixed above the water condensation level.

3.2. Retrieval Process

[22] The first step in the retrieval process is to define the background continuum between the gas absorption bands of interest. We make no attempt at any mineralogical interpretation of this continuum so it is not important to accurately model the surface phase function. We simply find the

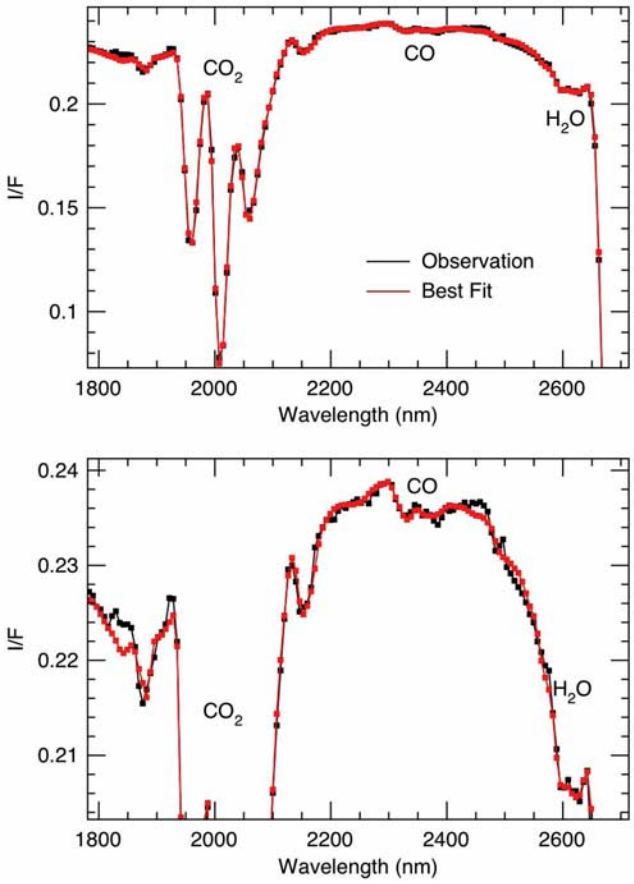

Figure 4. The best fit computed spectrum (red) compared against the CRISM observation (black) for the same spectrum (HRL0000515F) shown in Figure 2. Retrieved values are a surface pressure of 7.3 mbar, water vapor abundance of 21 pr μm, and carbon monoxide mixing ratio of 780 ppm.

equivalent albedo of a Lambert surface at wavelengths just outside gas bands and then linearly interpolate those values across the gas bands. While this approximation yields satisfactory results for the CO_2 band (2000 nm), it does not work as well for the CO band (2350 nm) because of weak absorption from water vapor on the long-wavelength side of the band, and it does not work at all for the H_2O band (2600 nm) because the long-wavelength side of this band is swamped by an extremely strong band of CO_2 centered at 2700 nm. Instead, an iterative approach is taken to define the continuum across the CO and H_2O bands as explained below.

[23] Once the continuum has been defined, the very strong and distinctive "triplet" appearance of the CO_2 band near 2000 nm (see Figure 2) allows an accurate retrieval of both the abundance of carbon dioxide and a wavelength calibration of the CRISM observation. We use 12 CRISM channels to define the peaks and edges of the band structure and fit for CO_2 abundance and wavelength calibration simultaneously. We model the wavelength calibration in a simple way as a single additive shift to the nominal wavelength of all CRISM channels. We have found that the wavelength for a given CRISM channel varies by as much as 1 nm and is roughly related to instrument temperature (warmer temperature gives a slightly higher wavelength for a given channel). Given that this amount of shift is an order of magnitude less than the spectral resolution of the observations, the wavelength shift is not important for many applications. Nevertheless, we have found that including this correction reduces the noise in our retrievals, especially for the very weak carbon monoxide band.

[24] Once the surface pressure (through carbon dioxide abundance) and the wavelength calibration have been established, we iteratively estimate the continuum level within the water vapor band and water vapor abundance. Beginning with a quick estimate of water vapor abundance based on a band depth formed from six CRISM channels within the water vapor band (2582, 2596, 2602, 2622, 2629, and 2642 nm) essentially defining the curvature of the observed spectrum near 2600 nm, we find the equivalent Lambert albedo for wavelengths on the low- and high-wavelength sides of the peak water vapor absorption (2582 and 2642 nm). The high-wavelength boundary is chosen as the last CRISM channel that is not overwhelmed by the CO_2 band centered near 2700 nm. The low-wavelength boundary is chosen to roughly center the peak of the observed water vapor band within the spectral interval. The albedo for intermediate wavelengths is estimated by linear interpolation between the two end values. A new retrieval of water vapor abundance is then performed using a full radiative transfer fitting of the spectrum in this spectral region. The new estimate of water vapor abundance is then used to find improved estimates of equivalent Lambert albedo and the process is iterated until convergence, which is generally very fast.

[25] The last step in the retrieval is the fitting for carbon monoxide abundance. As the CO band is very weak and also relatively weakly dependent on the abundance of CO, it is important to have the best estimates possible for all other quantities first. As in previous steps, the continuum level in the CO band is determined by solving for the equivalent Lambert albedo at wavelengths just outside the CO band, and then linearly interpolating the albedo values across the band. The CRISM channel used to define the continuum on the high-wavelength side of the CO band has a very small, but still noticeable contribution from water vapor absorption, which is taken into account using the retrieved water vapor abundance. Finally, we use 18 CRISM channels covering the entire CO band and its nearby continuum to fit for carbon monoxide abundance using our radiative transfer modeling.

3.3. Output Quantities

[26] The final output from the retrieval process is the abundances of carbon dioxide, carbon monoxide, and water vapor, a wavelength offset calibration, and equivalent Lambert albedo as a function of wavelength defining the continuum level. These quantities are output to a file along with additional data describing the quality of the fit for each parameter.

[27] Figure 4 shows the best fit synthetic spectrum to the same CRISM observation as shown previously in Figure 2 (HRL0000515F). For this observation, the retrieved quantities are a surface pressure of 7.3 mbar, wavelength offset from nominal of +0.34 nm, carbon monoxide mixing ratio

of 780 ppm, and water vapor column abundance of 21 precipitable micrometers (pr μm). The quality of this fit is good. We reject any retrieval with parameters outside reasonable bounds (e.g., surface pressure greater than 15 mbar), or whose fit is poor as determined by the rms difference between observed and best fit computed radiance. A poor fit is defined as the 5% of retrievals having the highest RMS radiance differences.

3.4. Uncertainties

[28] The formal uncertainties calculated by propagation of instrument noise are usually relatively small, with an exception being the case of carbon monoxide abundance. Of greater relevance are the uncertainties related to systematic errors in the assumptions and approximations used in the retrieval process. These uncertainties are best estimated by numerical experiment. For a given observation, the retrieval can be run for a range of different assumptions and approximations to evaluate the resulting change in the retrieved quantities. Using the typical observation HRL0000515F shown above in Figure 4, we describe below the results of several of these numerical experiments.

[29] One assumption in this retrieval is the use of aerosol optical depth derived from THEMIS observations instead of a value derived directly from the CRISM observation itself. For HRL0000515F, the THEMIS observations give a dust optical depth of 0.4 when converted to the wavelengths of interest (2000–2600 nm) using the dust indices of refraction derived by *Wolff et al.* [2009]. This is typical of non–dust storm conditions. Setting the optical depth of dust to zero, or doubling the THEMIS value leads to changes in the retrieved abundances of 3% for CO_2, 1% for H_2O, and 3% for CO. If we assume that there was actually a dust storm (dust optical depth of two, for example), then the errors become much more significant: 20% for CO_2, 6% for H_2O, and 15% for CO. Therefore, as long as the THEMIS observations are able to give generally accurate aerosol optical depth, and most importantly, to determine when and where large dust storms occurred, the uncertainties caused by our use of THEMIS aerosol optical depth will be relatively small. A related assumption is our use of a well-mixed dust. Numerical experiments show that taking different vertical distributions for the dust causes changes in retrieved quantities no larger than those quoted above.

[30] Another assumption is our use of TES climatology for the atmospheric temperature profile. Although thermal radiation is not important at the wavelengths considered here, the spectroscopic properties of the gases, including line strengths and widths, are temperature-dependent. We expect climatology atmospheric temperatures to almost always be within 10 K of the true value [*Smith*, 2004]. A shift of the climatology temperature profile by 10 K over the entire atmosphere leads to a change in the retrieved abundances of 1.5% for CO_2, 15% for H_2O, and 9% for CO. Somewhat surprisingly, the sensitivity to the assumed temperature profile appears to be greater than the sensitivity to assumed dust optical depth.

[31] Because the atmospheric temperature and pressure of the gas matters, there is also some sensitivity to the vertical distribution of water vapor. We have assumed that water vapor is well mixed to the water condensation level, but if we take an extreme case where all water vapor is confined to the lowest 3 km above the surface we see a change in retrieved water vapor column abundance of 10%.

[32] Another key assumption worth mentioning is the value used for the CO_2 broadening of water vapor and carbon monoxide lines. The broadening coefficients given in the HITRAN database are for terrestrial conditions (i.e., broadened by a nitrogen/oxygen mixture). Recent laboratory experiments by *Brown et al.* [2007] measured CO_2 broadening of water vapor in the thermal infrared, but there are still little or no measurements for broadening in the 2600 nm water vapor band. The theoretical work of *Gamache et al.* [1995] can be used, but numerical experiments show that in the thermal infrared using the CO_2 broadening coefficients measured by *Brown et al.* [2007] gives retrieved water vapor abundance that is less than 5% different than using the very simple formulation of *Smith* [2002], which was to multiply all terrestrial broadening coefficients by a constant factor of 1.5. Therefore, for simplicity we choose to use the constant multiplicative factor of 1.5 to estimate CO_2 broadening of water vapor lines. The uncertainty associated with this assumption is difficult to quantify, but is unlikely to be larger than the 10–20% values computed above, and in any case would give a nearly constant overall shift to retrieved values leaving seasonal and spatial patterns unaffected. In a similar way, for carbon monoxide we have multiplied all terrestrial broadening coefficients by a constant factor of 1.25 to approximate CO_2 broadening of CO [*Varanasi*, 1975; *Sung and Varanasi*, 2005].

[33] Uncertainty related to our approximation of the continuum level is more difficult to test experimentally. During the development of the retrieval process outlined in section 3.2, we experimented with many different ways to approximate the continuum level. The formulation that we chose was the one that consistently produced the best fits over the entire gas band, and that minimized the "noise" in retrieved quantities between observations spaced closely in time and location. On the basis of our experience with this and other retrievals, we believe that the choice of the continuum level is a significant but not dominant source of uncertainty, and is more important for weaker spectral signatures. We estimate the uncertainties as no more than 5% for CO_2, 10% for H_2O, and 20% for CO.

[34] Model-related assumptions, such as the number of vertical levels used to model the atmosphere, the number of streams used in the discrete ordinates, and the number of terms used in the Legendre polynomial expansion of the aerosol scattering phase function were tested by (for example) doubling the number of levels, streams, or terms in the expansion. All of these resulted in changes in retrieved abundances of less than 2%.

[35] The occurrence of a major dust storm is a special case and deserves additional comment. The typical total air mass for CRISM observations is typically between about 2.5 and 4 considering both the incidence and emergence of the radiation. During a major dust storm the line of sight optical depth becomes much greater than unity so that the dust screens the lower atmosphere and the entire column is not well sampled. In the time period considered in this study there was one planet-encircling dust storm that had very large optical depth between roughly $L_s = 270°$ and 305° (Mars Year 28, July–August 2007) north of about 40°S latitude (see Figure 3). Retrievals taken during this time of

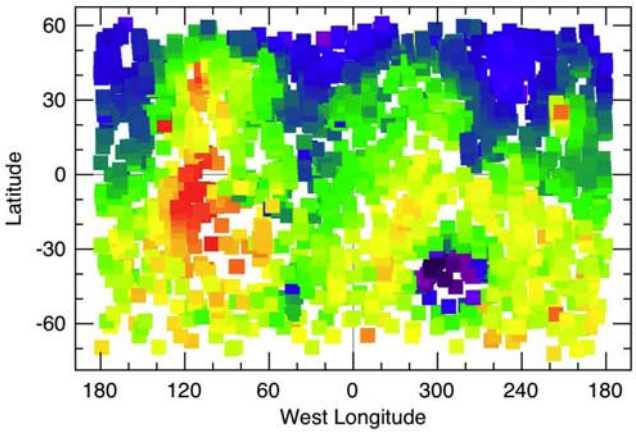

Figure 5. Map showing retrieved surface pressure for all retrievals between L_s = 0° and 30°. The scale is from 11 mbar (purple) to 3 mbar or lower (red).

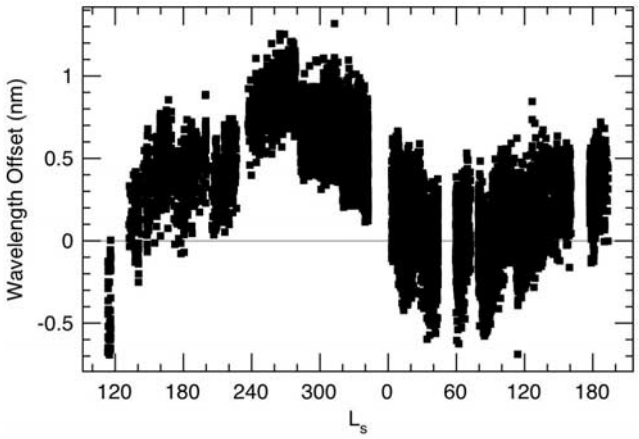

Figure 7. The retrieved wavelength calibration offset as a function of season (L_s). The offset is small compared with the spectral resolution (~15 nm), but including it improves the retrievals.

maximum dust loading will have significantly higher uncertainties, and in some cases should be disregarded completely.

[36] Considering all of the above sources of uncertainty, we estimate that the total uncertainty in gas abundance for a single retrieval as 10% for CO_2 (or surface pressure), 20% for H_2O, and 40% for CO. Spatial and temporal averaging can reduce these uncertainties by perhaps a factor of two or three, but part of the uncertainty is systematic and does not necessarily average out.

4. Results

[37] Here we present the results of retrievals of gas abundance performed on all CRISM EPF and hyperspectral nadir observations. The retrievals presented here cover a little more than one full Martian year of observations. Observations with a solar incidence angle greater than 80°, those showing the signature of surface ice, and those with the highest RMS residuals between best fit and computed radiance have been excluded leaving a total of 15,100 retrievals.

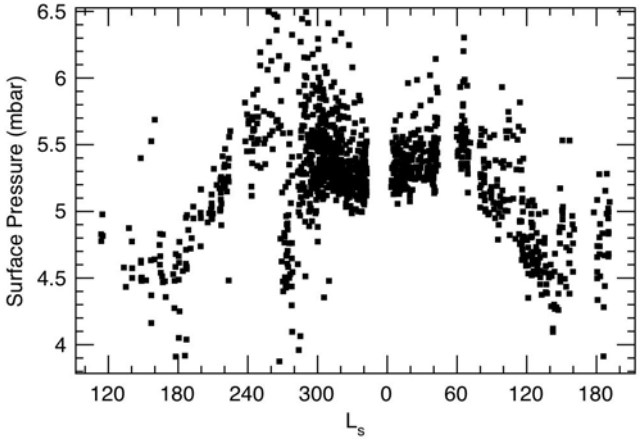

Figure 6. The retrieved surface pressure for all observations between MOLA elevations of +1.0 and +1.5 km above datum. The annual cycle of surface pressure is apparent, along with incorrect low values during the large dust storm (L_s = 270°–300°).

4.1. Surface Pressure

[38] Although the main goal of this paper is to describe the retrievals of water vapor and carbon monoxide, the retrieval of carbon dioxide (or equivalently, of surface pressure) is an important first step in the retrieval process and it is worthwhile to show the results to validate the rest of the retrieval. We have converted the abundance of carbon dioxide to a surface pressure using an assumed mixing ratio for CO_2 of 0.9532. Below, we will refer to the carbon dioxide abundance results in terms of surface pressure.

[39] Retrieved surface pressure shows the expected seasonal variation and direct relation to elevation. Figure 5 shows the spatial variation of surface pressure during a specific season (L_s = 0°–30°). Clearly visible are the topographic features of Hellas, Argyre, Tharsis, and the north-south hemisphere dichotomy. Figure 6 shows the seasonal variation of surface pressure for all observations in a given altitude interval as measured by MOLA [*Smith et al.*, 2001]. The observed annual cycle, with maximum surface pressure near L_s = 60° and 260° and minima near L_s = 0° and 160°, is consistent with the extensive record of the Viking Landers [*Tillman et al.*, 1993]. Also apparent in Figure 6 between L_s = 270° and 300° are incorrect low values taken during conditions with very high dust loading. These incorrect low values illustrate the difficulty of performing accurate gas abundance retrievals during major dust storms.

[40] Figure 7 shows the wavelength calibration offset, which is retrieved simultaneously with carbon dioxide abundance. The wavelength offset shows a clear seasonal variation that follows instrument temperatures. Warmer instrument temperatures during the perihelion season lead to a slight shift toward higher wavelengths, while colder instrument temperatures during the aphelion season lead to a slight shift toward lower wavelengths for a given CRISM channel. Much of the variation at a given seasonal date is related to the variation of instrument temperatures within a given orbit. The total amount of wavelength variation of

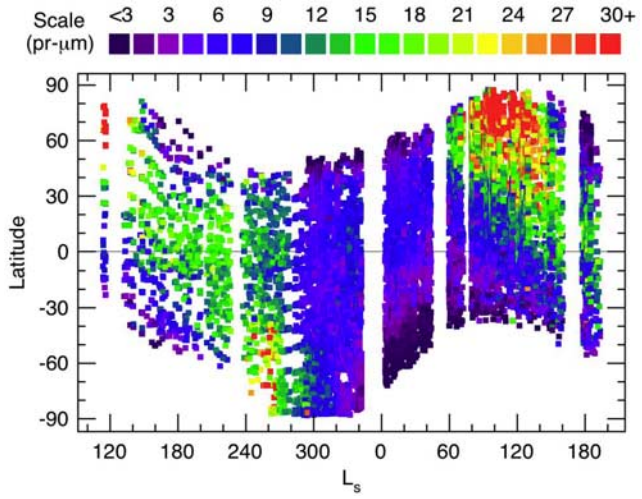

Figure 8. The column abundance of water vapor as a function of season (L_s) and latitude as observed by CRISM during Mars Years 28 and 29.

about 1.5 nm is relatively small compared to the spectral sampling (6.55 nm) and spectral resolution (~15 nm) at the wavelengths considered here (2000–2600 nm), but inclusion of this effect does result in a measurable improvement in retrieval results.

4.2. Water Vapor

[41] The retrieved column abundance of water vapor as a function of seasonal date (L_s) and latitude as observed by CRISM is shown in Figure 8. There are large differences in hemispheric (north versus south) and seasonal (aphelion versus perihelion) behavior of water vapor. A strong maximum in water vapor abundance is observed at high latitudes during northern hemisphere summer. Peak abundance of about 50 pr μm is obtained in both Mars Year 28 and 29 at $L_s = 110°–120°$ poleward of 60° N latitude. Water vapor abundance at high northern latitudes rapidly decreases after $L_s = 120°$, falling to levels below 10 pr μm by $L_s = 160°$. As water vapor abundance decreases at high northern latitudes, it continues to increase at low northern latitudes implying an equatorward transport of water vapor. Low northern latitude abundance builds to about 15 pr μm before falling off after $L_s = 220°$. In the southern hemisphere, a high-latitude summertime maximum is observed, but it is notably weaker than in the north, reaching an average of only about 25 pr μm. In the CRISM observations, the southern summertime maximum is abruptly cut off after $L_s = 270°$, and the entire southern hemisphere remains relatively dry (less than 5 pr μm) after $L_s = 0°$. Northern low latitudes maintain a somewhat higher water vapor abundance (5–10 pr μm) during northern Fall and Winter, with a rapid increase in water vapor beginning around $L_s = 50°$ building toward another summertime maximum.

[42] Figure 9 is a map showing all CRISM retrievals of water vapor taken between $L_s = 105°$ and 125° during the current Mars Year 29. This time period represents the peak of the northern hemisphere summertime maximum, and is also a time period for which we have a relatively large number of CRISM observations. Figure 9 (top) shows total water vapor column abundance, while Figure 9 (bottom) shows water vapor abundance scaled to an equivalent 6.1-mbar pressure level to remove the effect of topography. Beyond the strong north-to-south gradient in abundance (and scaled abundance), there is spatial structure in scaled water vapor that shows a positive correlation with surface albedo (bright regions have higher water vapor abundance), and negative correlations with thermal inertia. These relations have been noted before [*Jakosky and Farmer*, 1982; *Rosenqvist et al.*, 1992; *Smith*, 2002]. At low northern latitudes there is more water vapor from Tharsis westward across Amazonis Planitia and also across Arabia Terra. At higher northern latitudes there is a minimum in water vapor near 0° longitude.

4.3. Carbon Monoxide

[43] The retrieved column mixing ratio of carbon monoxide as a function of seasonal date and latitude as observed by CRISM is shown in Figure 10. Figure 10 (top) shows the actual retrieved values for each CRISM observation. As mentioned earlier, the retrieved CO mixing ratio is noisy because of the weakness of the CO absorption and the relatively weak dependence of the absorption on CO mixing ratio. To aid in the recognition of seasonal and spatial patterns, a smoothed version of the CO mixing ratio is shown in Figure 10 (bottom). The smoothing is performed by taking a box 15° in L_s by 15° in latitude centered on each point. The highest 30% and lowest 30% of all points in the box are discarded, and the smoothed value is given as the average of the median 40% of the points in the averaging box.

[44] Even without smoothing there are clear seasonal trends in the carbon monoxide mixing ratio. The summer-

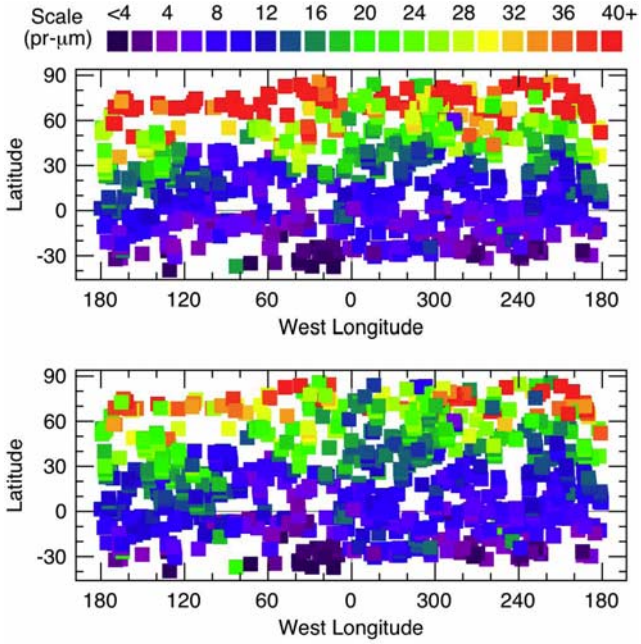

Figure 9. Maps of (top) total water vapor column abundance and (bottom) water vapor column abundance scaled to an equivalent 6.1-mbar pressure level to remove the effect of topography for the period $L_s = 105°–125°$.

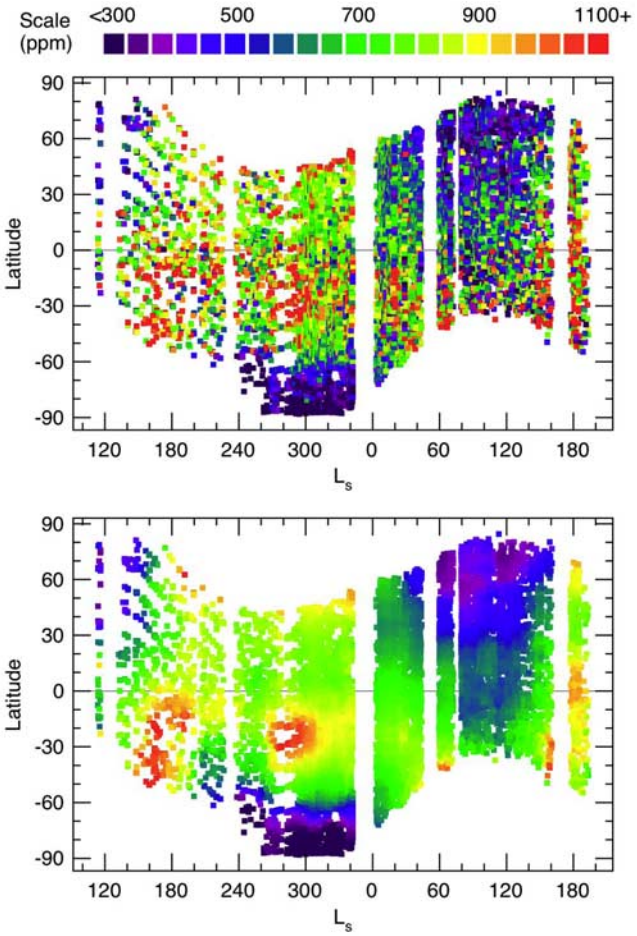

Figure 10. The mixing ratio of carbon monoxide as a function of season (L_s) and latitude as observed by CRISM during Mars Years 28 and 29. (top) Actual individual retrievals; (bottom) a smoothed representation of the data to more easily identify trends.

time polar regions in both hemispheres show very significant depletion in carbon monoxide. Compared against the seasonally and globally averaged value of 700 ppm observed by CRISM, CO mixing ratio falls to about 200 ppm between L_s = 280° and 300° poleward of 80°S latitude, and to 400 ppm (or perhaps somewhat less) near the north pole at summer solstice. There are fewer good retrievals near the north pole near solstice than in the south, so the minimum CO mixing ratio is more difficult to determine in the north. Unfortunately, CRISM observations in the winter polar regions are not possible when the Sun is below the horizon, but there are indications from the retrievals that a corresponding enhancement in CO mixing ratio exists near the winter pole.

[45] The southern hemisphere summertime depletion of CO shows a fairly well-defined boundary at about 60°S latitude and lasts from at least L_s = 235° until L_s = 0°. Although minimum mixing ratios in the north do not fall to the levels observed in the south, the northern hemisphere depletion is observed to cover a greater latitude extent. The northern depletion extends as far south as 30° N latitude, and is observed from L_s = 30° until L_s = 155°. Notable is the somewhat earlier phasing of the northern hemisphere depletion with respect to summer solstice.

[46] The enhancement in CO mixing ratio between L_s = 270° and 305° at 10°–40°S latitude corresponds very closely with the time and location of the planet-encircling dust storm (see Figure 3). Therefore, we believe this enhancement is an artifact caused by the difficulty in performing the retrieval under extreme dust loading and is not a real feature. However, the enhancement at L_s = 145°–200° is observed in both Mars Year 28 and 29, and it does appear to be a real response to the annual surface pressure minimum which occurs at this time (see Figure 6).

[47] Figure 11 presents maps showing the spatial distribution in latitude and longitude of CO mixing ratio for three different seasonal periods (L_s = 75°–105°, 135°–165°, and 240°–270°). The last of these periods was chosen to be just before the planet-encircling dust storm. Some spatial smoothing has been performed in an attempt to bring out spatial patterns. The smoothing is performed by taking a box 45° in longitude by 15° in latitude centered on each point. The highest 30% and lowest 30% of all points in the box are discarded, and the smoothed value is given as the average of the median 40% of the points in the averaging box. In addition to the clear latitudinal gradients, there also

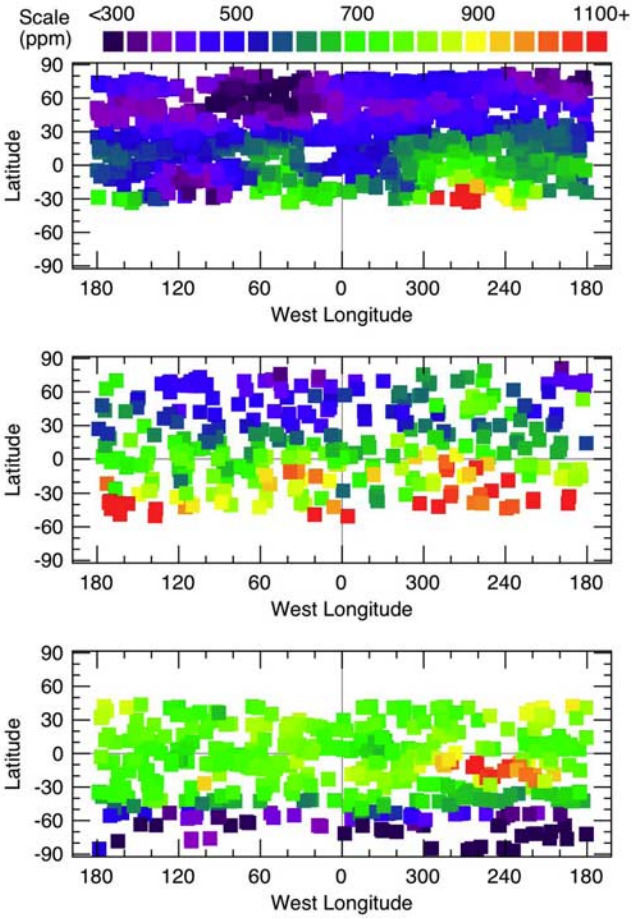

Figure 11. Maps of carbon monoxide mixing ratio for (top) L_s = 75°–105°, (middle) 135°–165°, and (bottom) 240°–270°. Some spatial smoothing has been performed to more easily identify patterns.

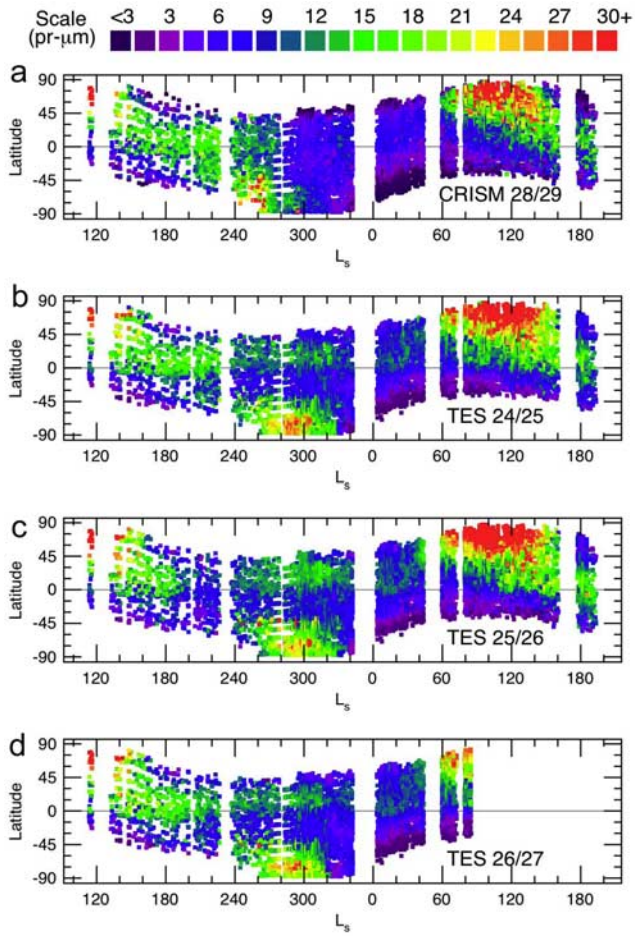

Figure 12. A comparison of the seasonal (L_s) and latitudinal dependence of water vapor as observed during 4 Martian years by CRISM and TES. Shown are (a) CRISM observations during Mars Years 28 and 29, (b) TES observations during Mars Years 24 and 25, (c) TES observations during Mars Years 25 and 26, and (d) TES observations during Mars Years 26 and 27.

appear to be regions with consistently higher mixing ratio such as the area north of Hellas Basin, and regions with consistently lower mixing ratio such as Acidalia Planitia. The lack of correlation with topography in the three maps supports our initial assumption that carbon monoxide is well mixed with the background CO_2 gas.

5. Discussion

5.1. Comparison of Water Vapor With Previous Observations

[48] The abundance of water vapor retrieved from CRISM observations presented above can potentially be directly compared against concurrent observations made by the Mars Climate Sounder instrument onboard MRO, and the Planetary Fourier Spectrometer (PFS), OMEGA, and SPICAM instruments onboard Mars Express [e.g., *Fouchet et al.*, 2007; *Tschimmel et al.*, 2008; *Melchiorri et al.*, 2007; *Maltagliati et al.*, 2008; *Fedorova et al.*, 2006]. However, at the time of this writing, there were no published retrievals of water vapor available from any of these instruments during the period of time observed by CRISM. Nevertheless, the CRISM observations can still be put into perspective by comparison against the long record of TES observations of water vapor [*Smith*, 2002, 2004, 2008].

[49] Figure 12 shows the seasonal and latitudinal dependence of water vapor as observed by CRISM (Mars Years 28/29) and by TES for each of its 3 Martian years of observations (Mars Years 24/25, 25/26, and 26/27). For ease of comparison, the TES results have been sampled at the same L_s and latitude locations as the CRISM observations. Overall, the seasonal and latitudinal patterns of water vapor are similar over the four Martian years shown here. Each shows a strong peak of water vapor in the northern hemisphere summer, water vapor spreading southward toward the equator as northern summer progresses, an increase in water vapor at high southern latitudes as southern spring ends, and low water vapor during the southern hemisphere fall and winter.

[50] However, there are also significant year-to-year differences apparent in Figure 12. The most obvious is lack of a southern hemisphere summertime maximum in water vapor in the CRISM observations after about $L_s = 270°$. The CRISM observations show an increase in southern hemisphere water vapor between $L_s = 200°$ and 270° that is similar in character and at least as strong as those observed by TES. But, while the TES observations from all 3 years show a continued increase in water vapor to a peak between $L_s = 280°$ and 300°, the CRISM observations show an abrupt drop in water vapor with continued low values into the southern Fall and Winter.

[51] The timing of the drop in southern hemisphere CRISM water vapor coincides with the onset of the 2007 planet-encircling dust storm (see Figure 3). An artifact in the TES water vapor retrievals caused by the 2001 planet-encircling dust storm [*Smith et al.*, 2002] can be seen in the form of lower water vapor abundances during Mars Year 25 between $L_s = 185°$ and 240° (Figure 12c). Likewise, CRISM water vapor retrievals may be artificially low during Mars Year 28, $L_s = 270°$ and 305°, however the highest dust optical depths from that storm remained north of 50°S latitude, and we believe that the CRISM water vapor retrievals poleward of that latitude were largely unaffected by the dust storm. The lack of a southern hemisphere summertime maximum by CRISM in Mars Year 28 represents a significant departure from previous results since the maximum was observed for Mars Years 24, 25, and 26 by TES [*Smith*, 2004], and for Mars Year 27 by Mars Express SPICAM [*Fedorova et al.*, 2006] and OMEGA [*Maltagliati et al.*, 2008]. However, none of the previous years (Mars Years 24–27) had planet-encircling dust storms at $L_s = 270°$ (the dust storm during Mars Year 25 was at $L_s = 185°$), which are known to produce significant changes to the atmospheric state [e.g., *Smith et al.*, 2002] and surface albedo [*Smith*, 2004]. A better comparison to previous results may be to the Viking Orbiter MAWD observations during Mars Year 12 (1977) [*Jakosky and Farmer*, 1982], when there was a planet-encircling dust storm near $L_s = 270°$ [*Martin and Richardson*, 1993]. The reanalysis of MAWD water vapor retrievals to account for the effect of dust by *Fedorova et al.* [2004] shows a somewhat similar behavior to that observed by CRISM. The buildup of

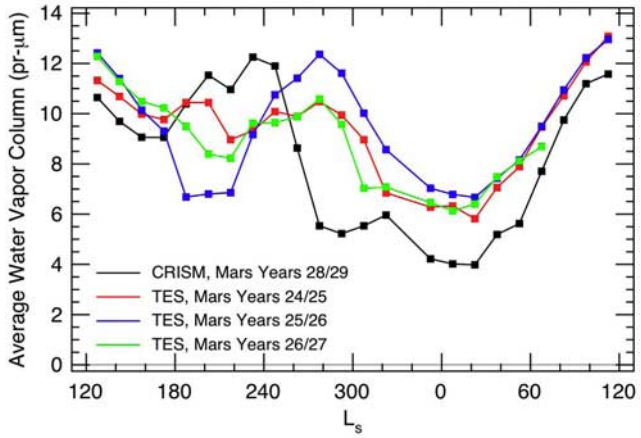

Figure 13. The globally averaged water vapor column abundance as a function of season (L_s) as observed during 4 Martian years by CRISM and TES.

southern hemisphere water vapor observed by Viking MAWD was nominal before the second planet-encircling dust storm of 1977 at $L_s = 275°$, but water vapor at high southern latitudes drops off quickly at $L_s = 280°$, after the onset of the dust storm. The best confirmation of the sharp dropoff in water vapor observed by CRISM will be comparisons against retrievals from concurrent Mars Express and MRO MCS observations when those results become available.

[52] The Mars Year 28 (2007) dust storm appears to have had a long-lasting effect on water vapor well after dust optical depth had returned to low, nominal levels. The CRISM observations show drier conditions planetwide after the dust storm until $L_s = 40°$, when water vapor levels in the northern hemisphere began to build again. Figure 13 shows globally averaged water vapor as a function of season for CRISM and the 3 TES years. The water vapor abundance observed by CRISM has a similar seasonal dependence, but a mild relative maximum between $L_s = 200°$ and 260° and a significantly deeper minimum between $L_s = 270°$ and 60°, with abundance 30–50% lower than observed by TES over that period. The CRISM observations are more similar to the very low water vapor abundance observed at $L_s = 345°$ during Mars Year 19 (1990) by *Clancy et al.* [1992] using ground-based microwave observations. Outside of the period between $L_s = 270°$ and 60°, the globally averaged water vapor abundances shown in Figure 13 agree reasonably well, although the CRISM results might possibly be biased low by 5–10% relative to the TES retrievals, which is well within the uncertainties of both retrievals.

5.2. Comparison of Carbon Monoxide With Previous Observations and Modeling Results

[53] Early ground-based observations of Mars in the microwave provided a good estimate of globally averaged CO mixing ratio of 600 ± 150 ppm (which is consistent with the results from CRISM presented here), and established that there are no large (>50%) variations in CO mixing ratio on a global scale [*Clancy et al.*, 1990]. Observations by *Krasnopolsky* [2003] using the IRTF/CSHELL long-slit spectrograph at $L_s = 112°$ showed a latitudinal gradient in CO mixing ratio, from 830 ppm north of 23° N latitude increasing to 1250 ppm at 45°S latitude. This hemispheric asymmetry was attributed to condensation of CO_2 gas in the southern polar region during the formation of the seasonal ice cap, which would lead to an enhancement in noncondensable species including carbon monoxide. CRISM observations during the same season show a similar trend, but lower values overall, with a CO mixing ratio of about 450 ppm poleward of 30° N latitude, increasing to the south reaching roughly 700 ppm at 30°S latitude. Observations by *Krasnopolsky* [2007] during the opposite season at $L_s = 312°$ showed the summertime depletion of CO at high southern latitudes (abundance of 1000 ppm in the northern hemisphere decreasing to 800 ppm at 80°S latitude), although the depletion is weaker than that observed by CRISM.

[54] The retrieval of the CO mixing ratio over Hellas basin by *Encrenaz et al.* [2006] using spectra from the Mars Express OMEGA instrument showed a clear seasonal variation that was consistent with a seasonal enrichment during southern winter caused by CO_2 condensation. Their retrieved CO mixing ratios are consistent with those retrieved from CRISM during southern hemisphere summer and fall ($L_s = 296°$ to 53°), but higher than CRISM during winter and spring ($L_s = 132°$ to 254°).

[55] This effect of enrichment by CO_2 condensation has also been observed by the Mars Odyssey GRS instrument in the form of a significant enhancement in the abundance of argon gas in the wintertime polar regions, especially in the south [*Sprague et al.*, 2004, 2007, also GRS measurements of Mars' atmospheric argon: Effects of updated Mars model atmospheres on concentration computations, paper presented at Third Workshop on Mars Modeling and Observations, Williamsburg, Virginia, 2008]. Further analysis of the argon measurements show how the observed variation of a noncondensable gas can provide important information about the general circulation on Mars. Modeling efforts have been able to reproduce the general characteristics of the observed enhancement of noncondensables [*Nelli et al.*, 2007; F. Forget et al., Non-condensable gas enrichment and depletion in the Martian polar regions, paper presented at Second Workshop on Mars Modeling and Observations, European Space Agency, Granada, Spain, 2006]. The models confirm that as CO_2 gas condenses and forms seasonal ice caps during the Fall season, the remaining noncondensable gases are "left behind" giving them an increased mixing ratio. The mixing of less enhanced air from lower latitudes can modify and limit this process [*Nelli et al.*, 2007].

[56] Although less abundant than argon by a factor of roughly 40, the CRISM observations show that a global and seasonal distribution of CO mixing ratio can be retrieved, and these results can provide similar information as a tracer of the atmospheric circulation. Because CRISM observations are made using reflected sunlight, we can only observe the polar regions during the spring and summer seasons. Instead of the wintertime enhancements observed in argon, we primarily observe the opposite season process of summertime depletion in CO. Presumably the physical process is the reverse of what happens in the winter. In this case, sublimation of the seasonal polar ice caps releases CO_2 into the atmosphere diluting the background noncondensable

gases including argon and carbon monoxide. Indeed, although not highlighted in their work, *Sprague et al.* [2007, also presented paper, 2008] do observe a depletion in argon over the summertime pole.

[57] As described earlier in section 4.3, CRISM observed a depletion of roughly 70% in the southern hemisphere summer, and a depletion of about 50% in the northern hemisphere summer. This is not inconsistent with the summertime depletion observed in argon by *Sprague et al.* [2007, also presented paper, 2008], although the stated uncertainties in the argon enhancement make a more conclusive statement impossible.

[58] Using the NASA Ames Mars General Circulation Model (GCM), *Nelli et al.* [2007] modeled the seasonal dependence of noncondensable gases to compare against the observed wintertime enhancement of argon. However, their results also show an expected depletion in argon over the summertime pole. Assuming that all noncondensable gases vary in a similar way, we can compare the CRISM carbon monoxide depletion against these model results. At 82.5°S latitude, the model results show an enhancement below unity between about L_s = 180° and 270°, with a minimum value of about 0.5. We do not have CRISM retrievals at that latitude before L_s = 260°, but the CRISM depletion appears significantly stronger than in the model, and lasts much later, until at least L_s = 330°. At 82.5° N latitude, the modeling by *Nelli et al.* [2007] shows an enhancement below unity between L_s = 15° and 110° with a minimum value of about 0.6, which again underestimates the strength and duration of the depletion in CO observed by CRISM.

[59] Results from the Mars GGM run at the Laboratoire de Météorologie Dynamique (LMD) also show depletion of noncondensable gases in the spring and summer polar regions (Forget et al., presented paper, 2008). The dependence of noncondensable gas mixing ratio on season and latitude given by the model has many similarities to the CO mixing ratio observed by CRISM. The biggest difference between the LMD model results and the CRISM observations is that the observations show the summertime depletion of CO persisting longer after the solstice than in the model, especially in the north.

6. Summary

[60] With over a full Martian year of observations now in hand, the results presented here using retrievals from CRISM spectra have extended the existing interannual record of water vapor abundance and have given the first description of the seasonal dependence of carbon monoxide mixing ratio over a wide latitude range.

[61] These retrievals reveal a seasonal water vapor cycle that is similar in many respects to that observed before by previous spacecraft, but also different in some important ways. The CRISM observations show the familiar northern hemisphere summertime maximum in water vapor (for both Mars Year 28 and 29) with a maximum column abundance of about 50 pr μm, and the subsequent migration of water vapor to low latitudes during the northern summer and fall. The increase in southern hemisphere water vapor during southern spring was nominal, but the CRISM retrievals after L_s = 270° show reduced water vapor abundance planetwide compared to observations from previous years. This includes a near absence of the southern hemisphere summertime polar maximum observed by TES and other instruments during previous years. It is likely not a coincidence that there was a planet-encircling dust storm at just the time when the water vapor abundances were observed to decrease, but it is beyond the scope of this paper to investigate such a connection in detail. Water vapor abundance observed by CRISM remained unusually low (compared against observations from previous years) until the springtime buildup of northern hemisphere water vapor, which appears nominal.

[62] The seasonal cycle of carbon monoxide is observed by CRISM to have large variations, which appear to be responses to the seasonal cycle of condensation and sublimation of CO_2 to and from the seasonal polar ice caps. The seasonal, global mean mixing ratio of carbon monoxide is about 700 ppm, but the mixing ratio drops to a minimum of about 200 ppm in the southern spring and summer high latitudes and to about 400 ppm in the northern spring and summer high latitudes as CO_2 sublimates from the seasonal ice cap and dilutes the noncondensable species such as carbon monoxide. CRISM observations rely on reflected sunlight and so are not possible over the winter poles, however some indication of the likely wintertime enrichment of carbon monoxide is indicated by the CRISM retrievals. The mean annual cycle of CO_2 abundance (or surface pressure) shows in the mixing ratio of carbon monoxide at low latitudes with highest values near L_s = 150° when surface pressure is lowest.

[63] Continued observations by CRISM will be useful to characterize the amount of interannual variability in the results shown here. Of particular interest will be to see whether in Mars Year 29 the southern hemisphere summertime maximum in water vapor abundance returns to its nominal strength as observed over many previous years, and the amount of variability in the carbon monoxide seasonal cycle, which has not been characterized at this level of detail before.

[64] **Acknowledgments.** We thank François Forget and Frank Lefèvre for helpful comments and for making modeling results on the seasonal and spatial variation of noncondensable gases available to us before their publication. The authors acknowledge financial support from the NASA Mars Reconnaissance Orbiter project as members of the CRISM Science Team and are grateful for all the hard work done by the CRISM operations team at the Applied Physics Laboratory who performed all the sequencing and calibration needed to obtain this data set.

References

Berk, A., L. S. Bernstein, G. P. Anderson, P. K. Acharya, D. C. Robertson, J. H. Chetwynd, and S. M. Adler-Golden (1998), MODTRAN cloud and multiple scattering upgrades with application to AVIRIS, *Remote Sens. Environ.*, *65*, 367–375.

Brown, L. R., C. M. Humphrey, and R. R. Gamache (2007), CO_2-broadened water in the pure rotation and ν_2 fundamental regions, *J. Mol. Spectrosc.*, *246*, 1–21.

Clancy, R. T., and S. W. Lee (1991), A new look at dust and clouds in the Mars atmosphere: Analysis of emission-phase-function sequences from global Viking IRTM observations, *Icarus*, *93*, 135–158.

Clancy, R. T., D. O. Muhleman, and G. L. Berge (1990), Global changes in the 0–70 km thermal structure of the Mars atmosphere derived from 1975 to 1989 microwave CO spectra, *J. Geophys. Res.*, *95*, 14,543–14,554.

Clancy, R. T., A. W. Grossman, and D. O. Muhleman (1992), Mapping Mars water vapor with the very large array, *Icarus*, *100*, 48–59.

Clancy, R. T., M. J. Wolff, and P. R. Christensen (2003), Mars aerosol studies with the MGS-TES emission phase function observations: Optical depths, particle sizes, and ice cloud types versus latitude and solar longitude, *J. Geophys. Res.*, *108*(E9), 5098, doi:10.1029/2003JE002058.

Encrenaz, Th., T. Fouchet, R. Melchiorri, P. Drossart, B. Gondet, Y. Langevin, J.-P. Bibring, F. Forget, and B. Bézard (2006), Seasonal variations of the Martian CO over Hellas as observed by OMEGA/Mars Express, *Astron. Astrophys.*, *459*, 265–270.

Fedorova, A. A., A. V. Rodin, and I. V. Baklanova (2004), MAWD observations revisited: Seasonal behavior of water vapor in the Martian atmosphere, *Icarus*, *171*, 54–67.

Fedorova, A. A., O. Korablev, J.-L. Bertaux, A. Rodin, A. Kiselev, and S. Perrier (2006), Mars water vapor abundance from SPICAM IR spectrometer: Seasonal and geographic distributions, *J. Geophys. Res.*, *111*, E09S08, doi:10.1029/2006JE002695.

Fouchet, T., et al. (2007), Martian water vapor: Mars Express PFS/LW observations, *Icarus*, *190*, 32–49.

Gamache, R. R., S. P. Neshyba, J. J. Plateaux, A. Barbe, L. Régalia, and J. B. Pollack (1995), CO_2-broadening of water vapor lines, *J. Mol. Spectrosc.*, *170*, 131–151.

Jakosky, B. M., and C. B. Farmer (1982), The seasonal and global behavior of water vapor in the Mars atmosphere: Complete global results of the Viking Atmospheric Water Detector Experiment, *J. Geophys. Res.*, *87*, 2999–3019.

Krasnopolsky, V. A. (2003), Spectroscopic mapping of Mars CO mixing ratio: Detection of north-south asymmetry, *J. Geophys. Res.*, *108*(E2), 5010, doi:10.1029/2002JE001926.

Krasnopolsky, V. A. (2007), Long-term spectroscopic observations of Mars using IRTF/CSHELL: Mapping of O_2 dayglow, CO, and search for CH_4, *Icarus*, *190*, 93–102.

Lacis, A. A., and V. Oinas (1991), A description of the correlated-k distribution method for modeling nongray gaseous absorption, thermal emission, and multiple scattering in vertically inhomogeneous atmospheres, *J. Geophys. Res.*, *96*, 9027–9063.

Lellouch, E., G. Paubert, and T. Encrenaz (1991), Mapping of CO millimeter-wave lines in Mars' atmosphere: The spatial variability of carbon monoxide on Mars, *Planet. Space Sci.*, *39*, 219–224.

Maltagliati, L., D. V. Titov, T. Encrenaz, R. Melchiorri, F. Forget, M. Garcia-Comas, H. U. Keller, Y. Langevin, and J.-P. Bibring (2008), Observations of atmospheric water vapor above the Tharsis volcanoes on Mars with the OMEGA/MEX imaging spectrometer, *Icarus*, *194*, 53–64.

Martin, T. Z., and M. I. Richardson (1993), New dust opacity mapping from Viking infrared thermal mapper data, *J. Geophys. Res.*, *98*, 10,941–10,949.

McGuire, P. C., et al. (2008), CRISM retrieval of surface Lambert albedos for multispectral mapping of Mars with DISORT-based radiative transfer modeling: Phase 1 – Using historical climatology for temperatures, aerosol optical depths, and atmospheric pressures, *IEEE Trans. Geosci. Remote Sens.*, *46*, 4020–4040.

Melchiorri, R., et al. (2007), Water vapor mapping on Mars using OMEGA/Mars Express, *Planet. Space Sci.*, *55*, 333–342.

Murchie, S., et al. (2007), Compact Reconnaissance Imaging Spectrometer for Mars (CRISM) on Mars Reconnaissance Orbiter (MRO), *J. Geophys. Res.*, *112*, E05S03, doi:10.1029/2006JE002682.

Nelli, S. M., J. R. Murphy, A. L. Sprague, W. V. Boynton, K. E. Kerry, D. M. Janes, and A. E. Metzger (2007), Dissecting the polar dichotomy of the noncondensable gas enhancement on Mars using the NASA Ames Mars General Circulation Model, *J. Geophys. Res.*, *112*, E08S91, doi:10.1029/2006JE002849.

Owen, T., K. Biemann, D. R. Rushneck, J. E. Biller, D. W. Howarth, and A. L. Lafleur (1977), The composition of the atmosphere at the surface of Mars, *J. Geophys. Res.*, *82*, 4635–4639.

Pelkey, S. M., et al. (2007), CRISM multispectral summary products: Parameterizing mineral diversity on Mars from reflectance, *J. Geophys. Res.*, *112*, E08S14, doi:10.1029/2006JE002831.

Rosenqvist, J., P. Drossart, M. Combes, T. Encrenaz, E. Lellouch, J.-P. Bibring, S. Erard, Y. Langevin, and E. Chassefière (1992), Minor constituents in the Martian atmosphere from the ISM/Phobos experiment, *Icarus*, *98*, 254–270.

Rothman, L. S., et al. (2005), The *HITRAN* 2004 molecular spectroscopic database, *J. Quant. Spectrosc. Radiat. Transfer*, *96*, 139–204.

Smith, D. E., et al. (2001), Mars Orbiter Laser Altimeter (MOLA): Experiment summary after the first year of global mapping of Mars, *J. Geophys. Res.*, *106*, 23,689–23,722.

Smith, M. D. (2002), The annual cycle of water vapor on Mars as observed by the Thermal Emission Spectrometer, *J. Geophys. Res.*, *107*(E11), 5115, doi:10.1029/2001JE001522.

Smith, M. D. (2004), Interannual variability in TES atmospheric observations of Mars during 1999–2003, *Icarus*, *167*, 148–165.

Smith, M. D. (2008), Spacecraft observations of the Martian atmosphere, *Annu. Rev. Earth Planet. Sci.*, *36*, 191–219.

Smith, M. D., J. C. Pearl, B. J. Conrath, and P. R. Christensen (2002), Thermal Emission Spectrometer observations of Martian planet-encircling dust storm 2001a, *Icarus*, *157*, 259–263.

Smith, M. D., J. L. Bandfield, P. R. Christensen, and M. I. Richardson (2003), Thermal Emission Imaging System (THEMIS) infrared observations of atmospheric dust and water ice cloud optical depth, *J. Geophys. Res.*, *108*(E11), 5115, doi:10.1029/2003JE002115.

Sprague, A. L., W. V. Boynton, K. E. Kerry, D. M. Janes, D. M. Hunten, K. J. Kim, R. C. Reedy, and A. E. Metzger (2004), Mars' south polar Ar enhancement: A tracer for south polar seasonal meridional mixing, *Science*, *306*, 1364–1367.

Sprague, A. L., W. V. Boynton, K. E. Kerry, D. M. Janes, N. J. Kelly, M. K. Crombie, S. M. Nelli, J. R. Murphy, R. C. Reedy, and A. E. Metzger (2007), Mars' atmospheric argon: Tracer for understanding Martian atmospheric circulation and dynamics, *J. Geophys. Res.*, *112*, E03S02, doi:10.1029/2005JE002597.

Sung, K., and P. Varanasi (2005), CO_2-broadened half-widths and CO_2-induced line shifts of $^{12}C^{16}O$ relevant to the atmospheric spectra of Venus and Mars, *J. Quant. Spectrosc. Radiat. Transfer*, *91*, 319–332.

Thomas, G. E., and K. Stamnes (1999), *Radiative Transfer in the Atmosphere and Ocean*, Cambridge Univ. Press, Cambridge, U. K.

Tillman, J. E., N. C. Johnson, P. Guttorp, and D. B. Percival (1993), The Martian annual atmospheric pressure cycle: Years without great dust storms, *J. Geophys. Res.*, *98*, 10,963–10,971.

Tschimmel, M., N. I. Ignatiev, D. V. Titov, E. Lellouch, T. Fouchet, M. Giuranna, and V. Formisano (2008), Investigation of water vapor on Mars with PFS/SW of Mars Express, *Icarus*, *195*, 557–575.

Varanasi, P. (1975), Measurement of line widths of CO of planetary interest at low temperatures, *J. Quant. Spectrosc. Radiat. Transfer*, *15*, 191–196.

Wolff, M. J., R. T. Clancy, M. D. Smith, R. Arvidson, M. Kahre, F. Seelos IV, and R. V. Morris (2009), Wavelength dependence of dust aerosol single scattering albedo as observed by Compact Reconnaissance Imaging Spectrometer, *J. Geophys. Res.*, doi:10.1029/2009JE003350, in press.

Zurek, R. W., and S. E. Smrekar (2007), An overview of the Mars Reconnaissance Orbiter (MRO) science mission, *J. Geophys. Res.*, *112*, E05S01, doi:10.1029/2006JE002701.

R. T. Clancy and M. J. Wolff, Space Science Institute, 4750 Walnut Street, Boulder, CO 80301, USA.

S. L. Murchie, Johns Hopkins University Applied Physics Laboratory, 11100 Johns Hopkins Road, Laurel, MD 20723, USA.

M. D. Smith, NASA Goddard Space Flight Center, Mail Code 693, Greenbelt, MD 20771, USA. (Michael.D.Smith@nasa.gov)